Science Advances
AAAS

advances.sciencemag.org/cgi/content/full/6/50/eabd2928/DC1

Supplementary Materials for

Physical origin of glass formation from multicomponent systems

Yuan-Chao Hu and Hajime Tanaka*

*Corresponding author. Email: tanaka@iis.u-tokyo.ac.jp

Published 11 December 2020, *Sci. Adv.* **6**, eabd2928 (2020)
DOI: 10.1126/sciadv.abd2928

This PDF file includes:

Figs. S1 to S10

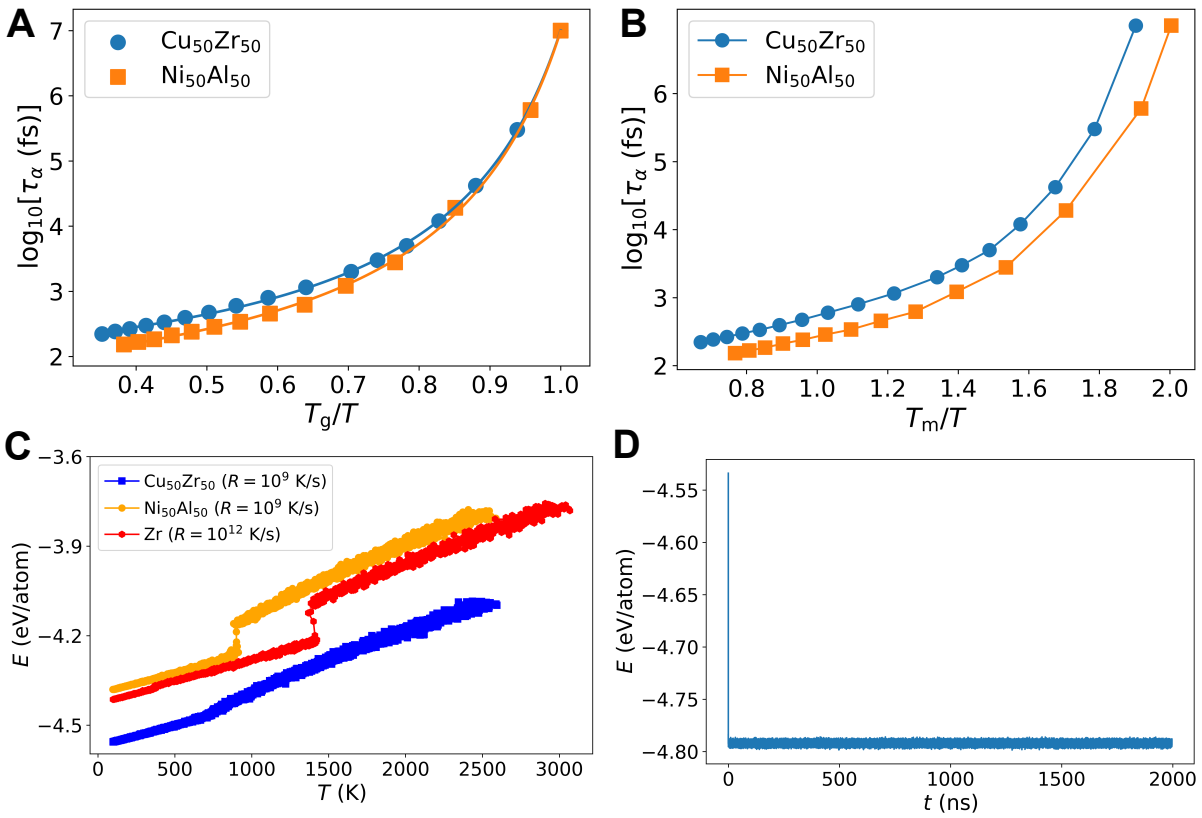

Fig. S1. **Liquid dynamics and potential energy change during cooling.** (**A**) The growth of the structural relaxation times τ_α upon cooling. The temperature is scaled by the glass-transition temperature T_g. The solid curves are fits to the VFT equation. (**B**) The growth of τ_α upon cooling. Here the temperature is scaled by the melting temperature T_m. (**C**) The potential energy per atom E during cooling for the three studied materials at certain cooling rates R. The data of CuZr and Zr were shifted by 0.35 and 2.0 for clarity. A first-order phase transition, i.e., crystallization, happens for NiAl and Zr, but CuZr only shows glass transition. (**D**) The temporal change in E of CuZr during annealing at 800 K ($0.6T_\mathrm{m}$). Similar results are obtained from three independent simulations.

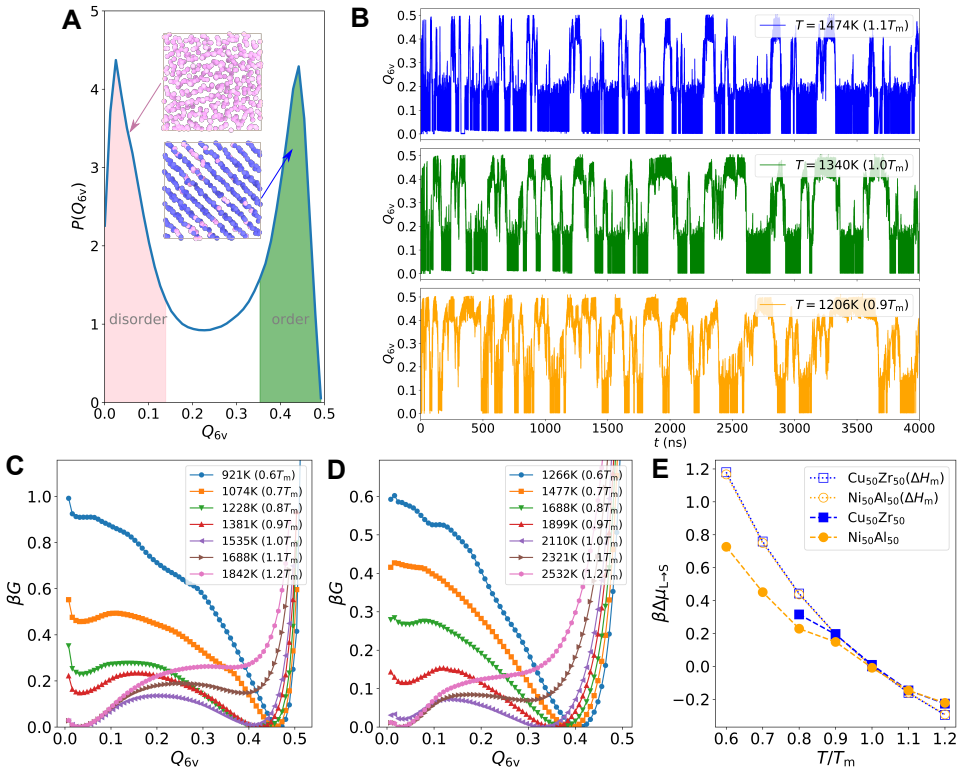

Fig. S2. **The collective variable and free energy profiles by well-tempered metadynamics.** (**A**) The probability distribution of the collective variable Q_{6v} obtained by simulations for CuZr at T_m. There are two distinct peaks corresponding to the liquid and the crystal phases, which are exemplified by the two atomic configurations. Blue and pink atoms indicate B2/bcc and disordered structures, respectively. (**B**) The temporal change of Q_{6v} for CuZr at three temperatures. As expected, when $T = T_m$, there is an equal chance to be in the liquid and crystal phases. On the other hand, the crystal and liquid phases are more preferred at $T < T_m$ and $T > T_m$, respectively. Most importantly, the observed diffusive behavior of the phase transition proves the convergence of the free-energy profiles. Similar behaviors have also been observed at other temperatures and for NiAl and Zr. (**C, D**) Free-energy profiles obtained by converged well-tempered metadynamics at various T/T_m for NiAl (**C**) and Zr (**D**). The free energy G is scaled by the thermal energy k_BT and the number of atoms. Obviously, at T_m, there is no Gibbs free-energy difference between the liquid and the crystal phases. For $T > T_m$, the liquid phase is more stable, whereas the crystal phase becomes more stable for $T < T_m$. (**E**) Comparison of the thermodynamic driving force. The filled symbols are the results of well-tempered metadynamics simulations. The open ones are estimated from the enthalpy of fusion (ΔH_m) measured by MD simulations (Refs. 18 and 37 in the main text). For the simulated CuZr and NiAl, $\Delta H_m/k_BT_m$ is 1.77 and 1.75, respectively (Ref. 37 in the main text). It is obvious that at small undercooling, both methods show similar values. However, the simple estimation from ΔH_m tends to overestimate $\Delta\mu_{L\to S}$ at large supercooling.

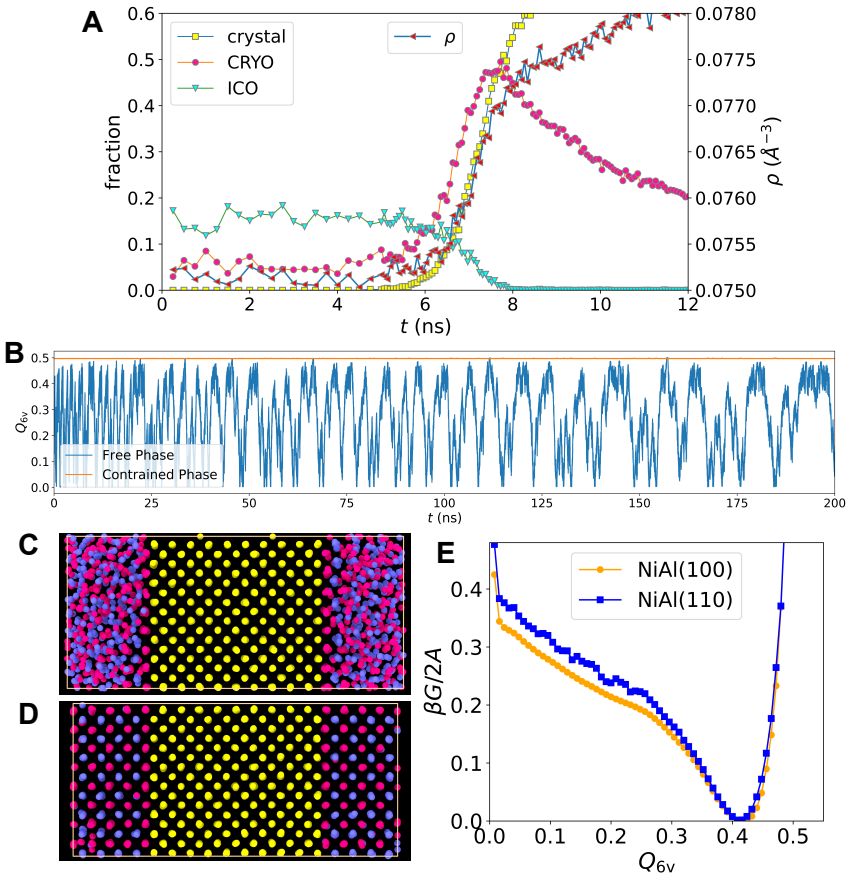

Fig. S3. **Spontaneous crystallization process and interface-energy calculation for NiAl.** (**A**) Time dependence of the fractions of crystal, CRYO, and ICO together with the density ρ during spontaneous crystallization in NiAl at the nose temperature. Crystal represents the crystallized atoms, while CRYO and ICO denote the atoms in the crystal-like and icosahedral environments, respectively. ρ is the number density. (**B**) The variation of the collective variable Q_{6v} of the constrained-solid and the free-liquid phases during the simulations for NiAl. As designed, the solid phase (yellow atoms in (**C**) and (**D**)) is restrained in the crystalline state with the invariant collective variable (constrained phase). On the other hand, for the liquid phase (free phase), its collective variable reversibly changes between the two states, indicating the diffusive behavior. (**C**) and (**D**) are configurations corresponding to the two states revealed in (**B**). Blue and pink represent different atomic species. (**E**) The free energy profiles of NiAl with the presence of planar crystal-liquid interfaces along different crystallographic planes (100) and (110). The meaning of the variables is the same as in Fig. 1E in the main text.

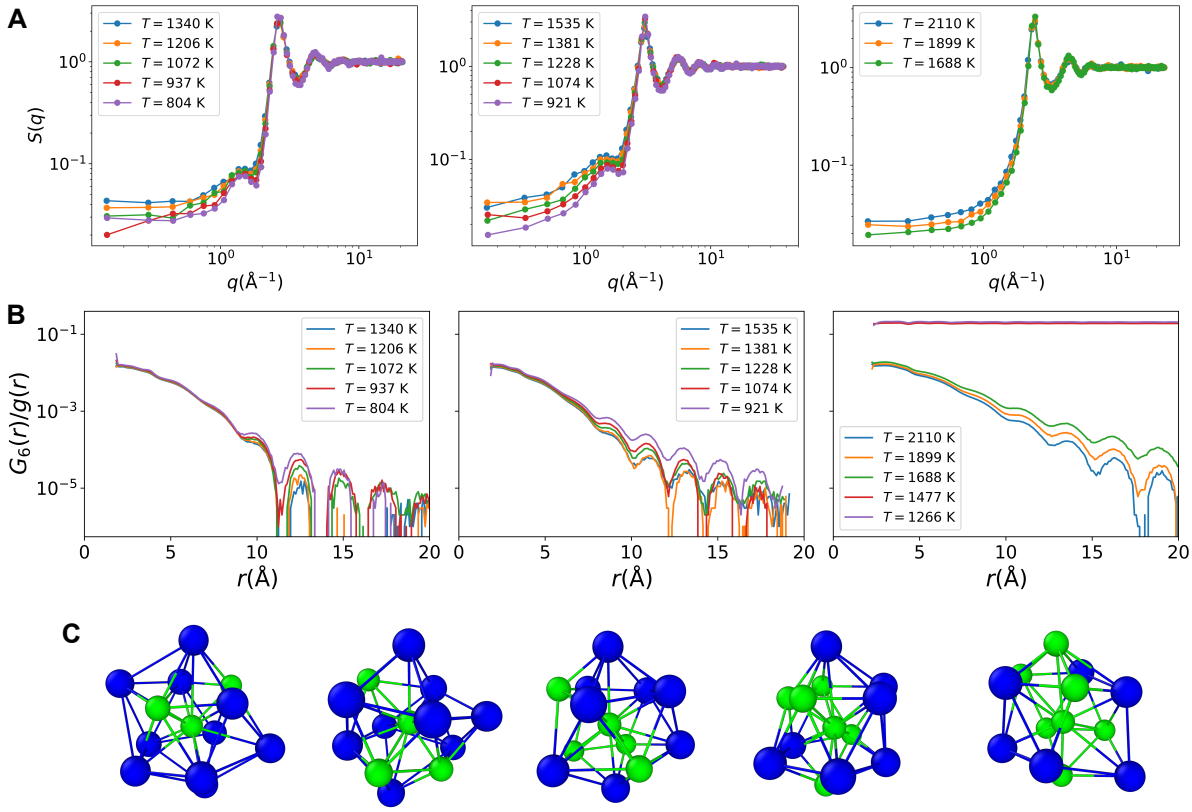

Fig. S4. **Spatial correlations of density and bond orientational ordering during cooling, and local icosahedral structure with various chemical orders.** (**A**) Static structure factor $S(q)$ for CuZr, NiAl, and Zr from left to right. $S(q)$ shows typical features of supercooled liquids without any extra scattering at low wavenumbers. It indicates that there is no crystallization happening. (**B**) Spatial correlation of the bond orientational order parameter for CuZr, NiAl, and Zr from left to right. The spatial correlation is calculated as $G_6(r)/g(r) = \frac{4\pi}{13}\frac{\sum_{i,j}\sum_{m=-6}^{6} Q_{6m}(i)Q^*_{6m}(j)\delta(r_{ij}-r)}{\sum_{i,j}\delta(r_{ij}-r)}$, whose spatial decay rate can quantify the correlation length of CRYO. Obviously, there is almost no such growth of the correlation length for CuZr upon cooling. However, the increasing trend of the correlation length upon cooling for Zr is remarkable until crystallization occurs below $0.8T_{\mathrm{m}}$. Therefore, the system is more prone to crystallization in the order of Zr, NiAl, and CuZr. (**C**) Typical atomic configurations of ICO around Cu in CuZr. Large blue atoms are Zr, while small green ones are Cu. The bonds are shown based on the first minimum position from the partial pair correlation functions. These results indicate the important roles of chemical ordering in determining the properties of the locally favored structures. The same topology can show significantly different properties.

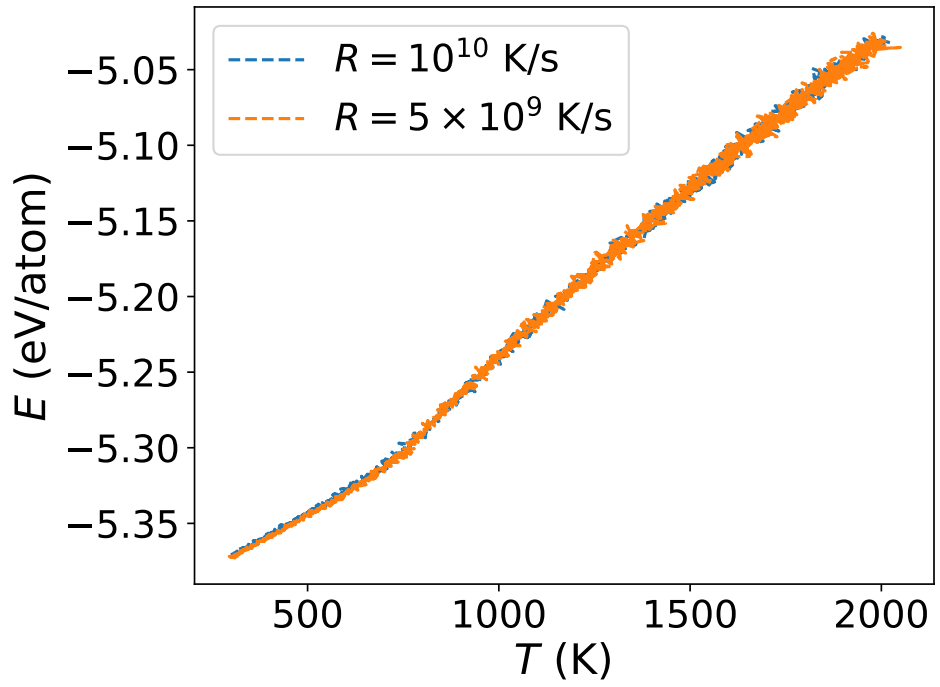

Fig. S5. **Temperature dependence of the potential energy at different cooling rates R for $CuZr_2$.** Similar results are obtained in 5 independent simulations. Obviously, R_c of $CuZr_2$ should be smaller than the shown R, which demonstrates the better GFA of $CuZr_2$ than NiAl with $R_c = 10^{9.9}$ K/s.

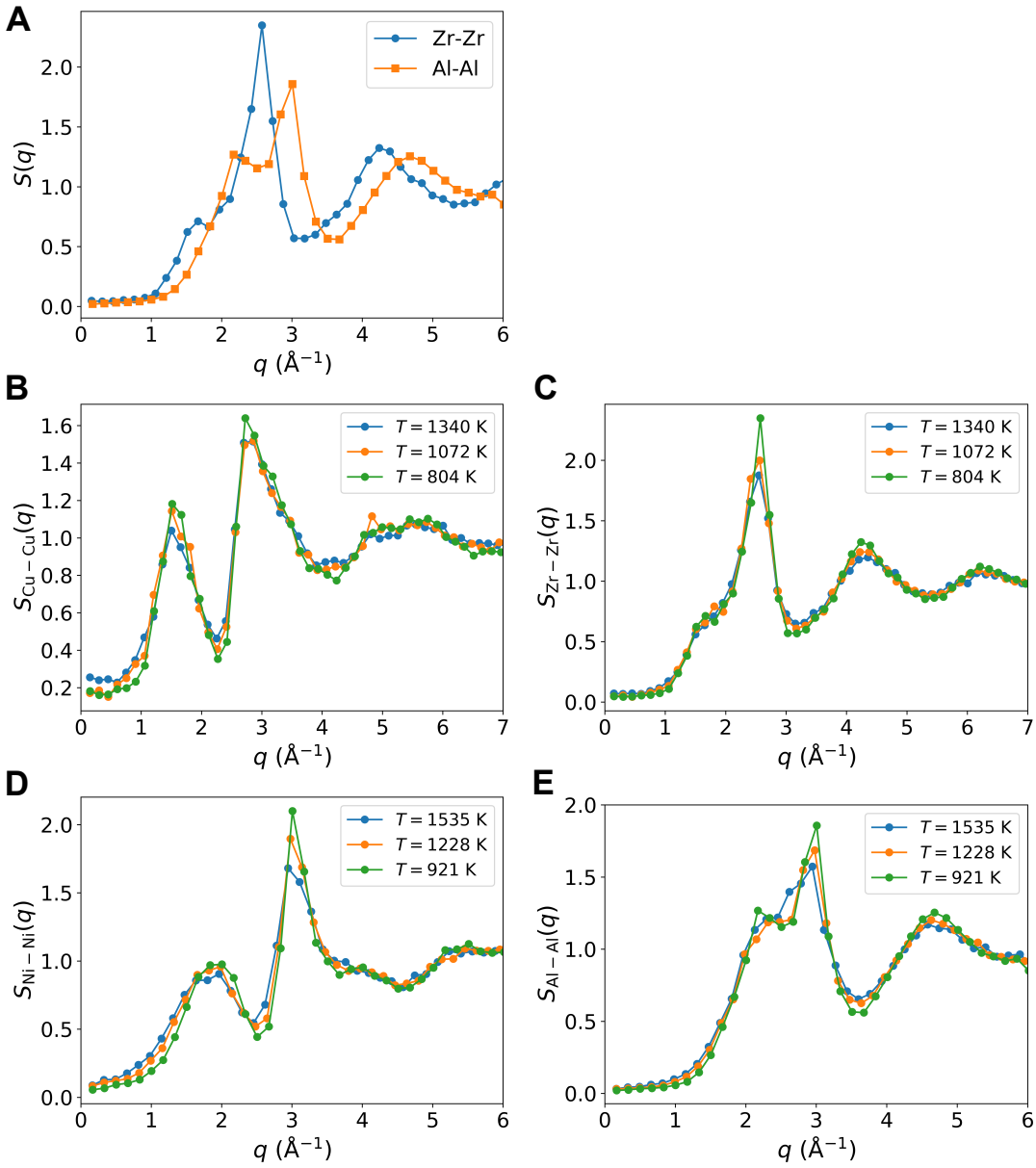

Fig. S6. **Partial structure factors and pre-peaks in supercooled liquids.** (**A**) Comparison of partial structure factors of Zr-Zr pair of CuZr and Al-Al pair of NiAl at $0.6T_{\mathrm{m}}$. The pre-peak before the main peak indicates the chemical ordering of the individual species. The characteristic lengthscale of concentration fluctuations of Zr-Zr is larger than Al-Al. Combining with Fig. 4B in the main text, it is not difficult to find that concentration fluctuations in CuZr are stronger than NiAl, which contributes to the better GFA of CuZr. (**B** to **E**) Temperature dependence of the partial structure factors for Cu-Cu, Zr-Zr, Ni-Ni, and Al-Al pairs. Obviously, the chemical ordering effect indicated by the presence of the pre-peak is only weakly dependent on the temperature. This evidences the stability and the significance of chemical ordering in supercooled metallic liquids.

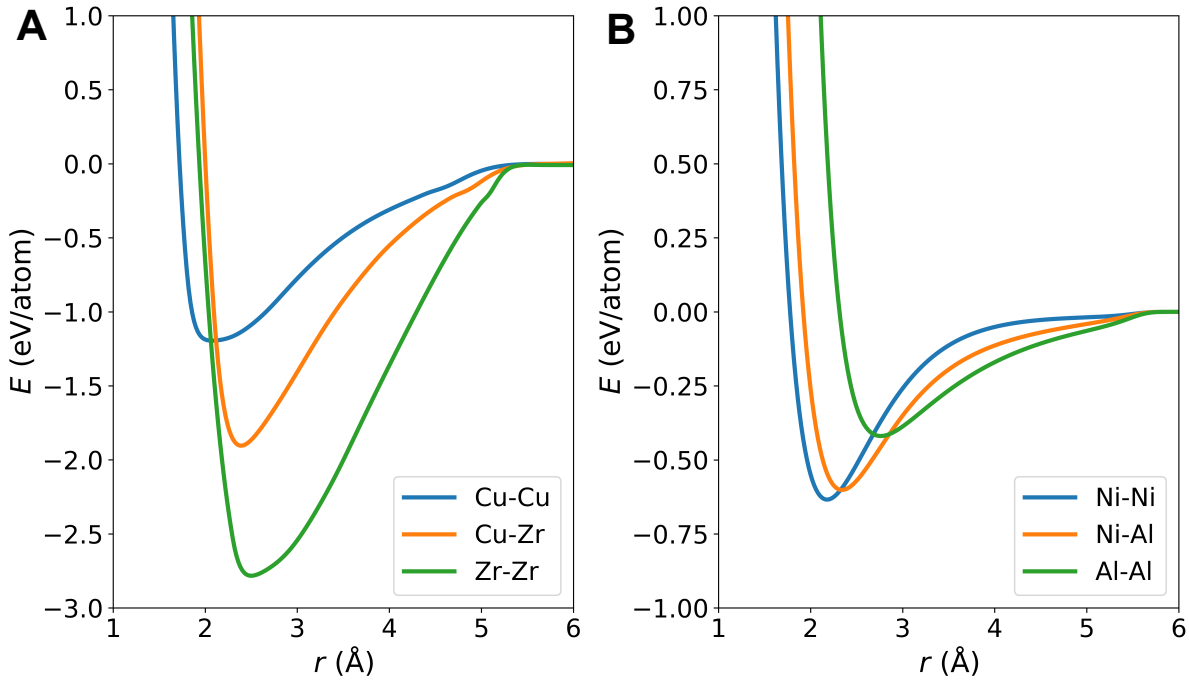

Fig. S7. **The effective pairwise potential of the many-body EAM potentials.** The diatom potential energy as a function of interatomic spacing associated with the EAM potentials for CuZr (**A**) and NiAl (**B**) respectively. They can be treated as the effective two-body interactions of the many-body EAM potential. Remarkably, (**A**) and (**B**) show quite different features. In CuZr, the Zr-Zr interaction is the strongest, while that of Cu-Cu is the weakest. Meanwhile, these pair interactions differ largely from each other. From the potentials, we can see that chemically, Cu prefers to have Zr as the nearest neighbors, and Zr also likes itself the most. This chemical preference is the origin of strong chemical ordering in a supercooled liquid, as discussed in the main text. However, in NiAl, the difference between different pairs is small, and the interactions are weaker than those of CuZr. Therefore, NiAl shows much weaker chemical ordering. Furthermore, the small difference of the pair potentials indicates a smaller barrier to form the targeted B2 crystal with Ni:Al=1:1.

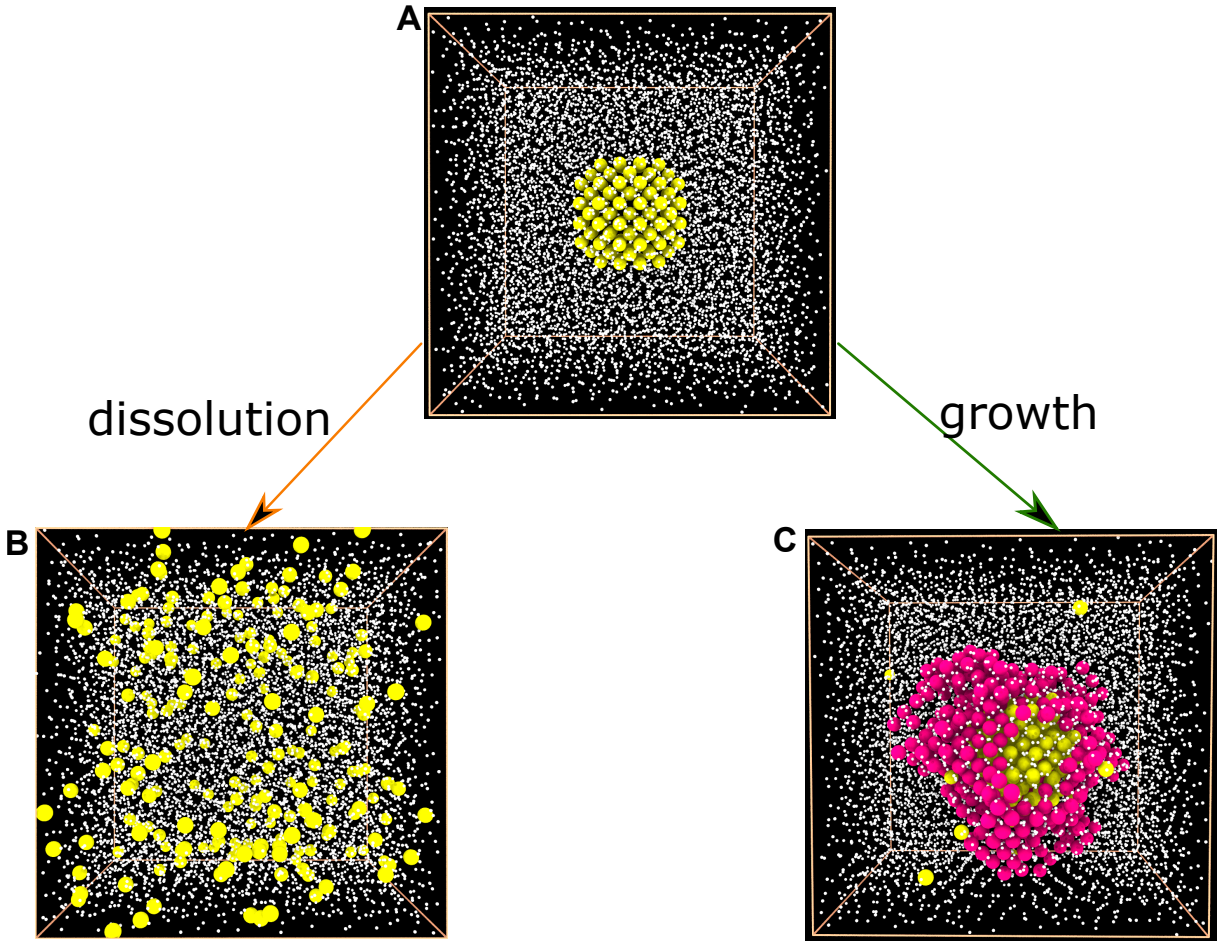

Fig. S8. **Evolution of a critical nucleus during isothermal annealing by the seeding simulations.** (**A**) Initial configuration of a crystalline seed with the critical nucleus size embedded in a supercooled liquid. The yellow atoms and white dots represent the seed and the liquid, respectively. The size of atoms has been adjusted for visualization. (**B**) The critical nucleus dissolves. (**C**) The critical nucleus grows. Yellow atoms and white dots in (**B**) and (**C**) represent atoms that initially belong to the seed and the liquid, respectively. The magenta atoms in (**C**) are newly attached atoms to the crystal nucleus, indicating crystal growth. Naturally, some yellow atoms in (**C**) are melt into the liquid. This result demonstrates the validity of the seeding method to study the crystallization kinetics in supercooled metallic liquids.

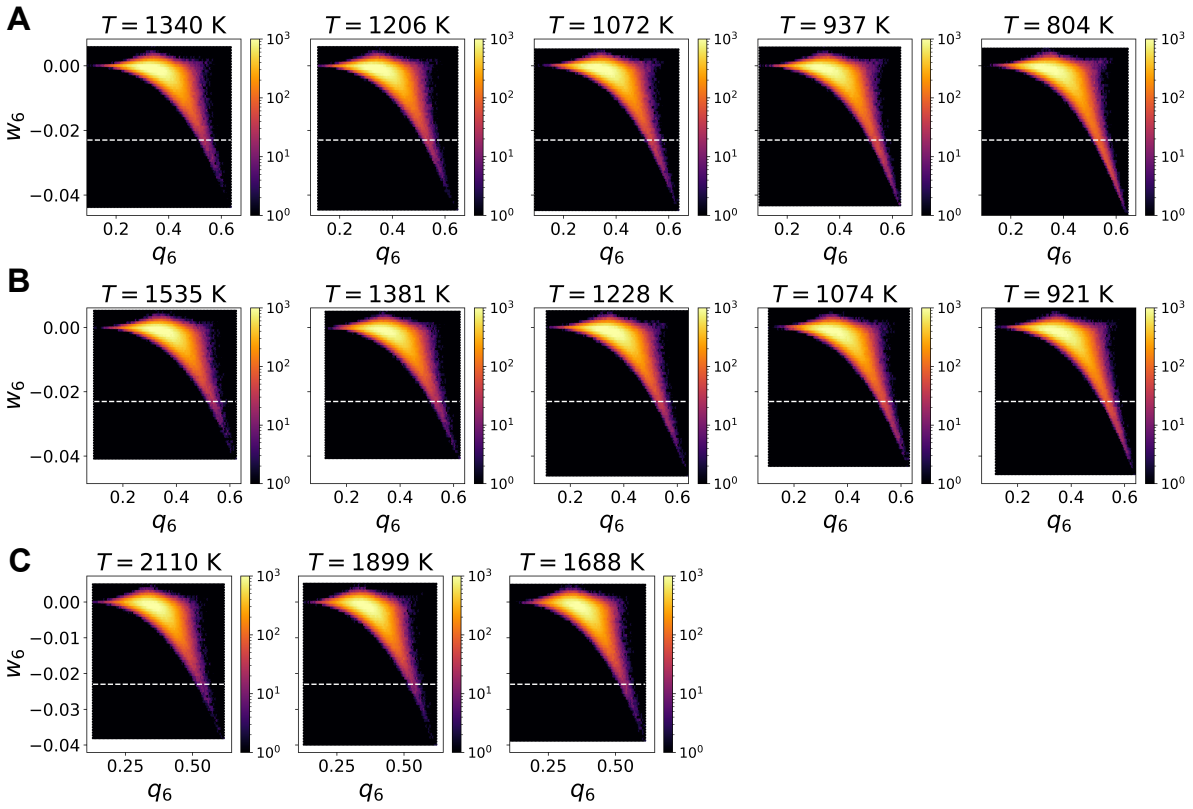

Fig. S9. $w_6 - q_6$ **map in supercooled liquids.** (**A**) CuZr. (**B**) NiAl. (**C**) Zr. The left column represents the temperature at T_{m}. These figures clearly demonstrate that atoms with large q_6 values also have low negative value of w_6, indicating the local icosahedral environment. The white dash line indicates the threshold value -0.023 to quantify icosahedral structures. It is obvious that the fraction of icosahedral ordering grows upon cooling in three materials, but the rate of the increase is different with each other.

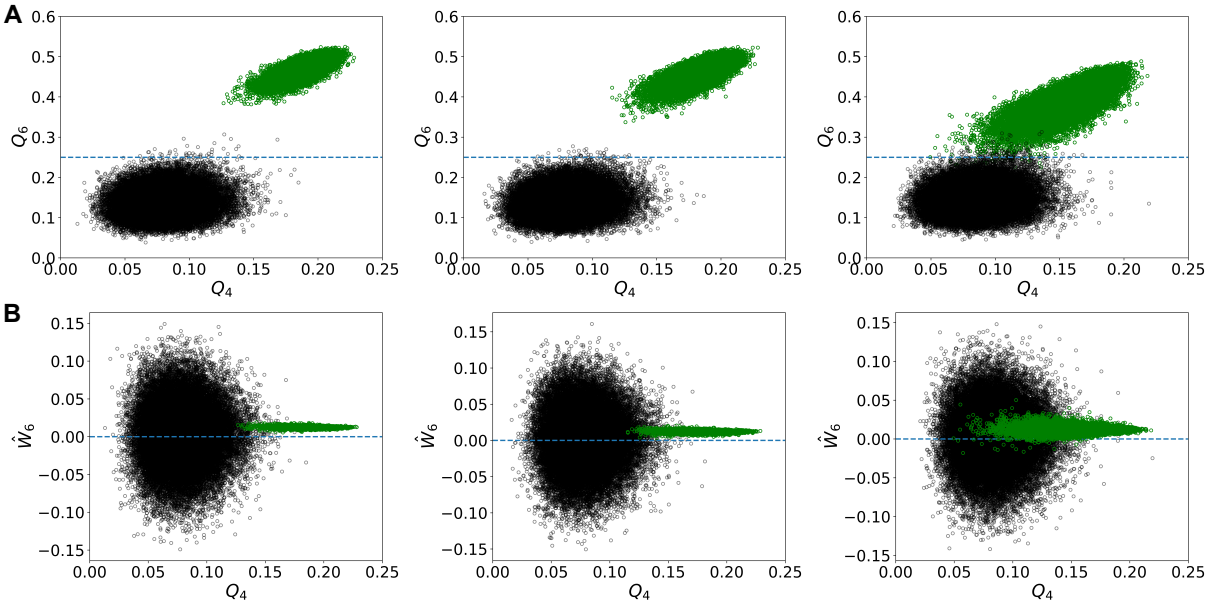

Fig. S10. **Maps of crystal-like bond orientational order parameters in liquids and crystals.** (**A**) $Q_6 - Q_4$ map at T_m. (**B**) $\hat{W}_6 - Q_4$ map at T_m. Green points represent equilibrium bcc/B2 perfect crystals, while the black dots depict equilibrium liquids. From left to right in each row, the samples are CuZr, NiAl, and Zr. The threshold value $Q_6 = 0.25$ (dashed line) can generally separate ordered particles from disordered ones. Moreover, even though the liquid structure shows both positive and negative values of $\hat{W}_6$, bcc crystal tends to have positive values. Therefore, the combination of these parameters can nicely separate the crystal-like bond orientational orderings with bcc-like symmetry from the liquid state.